

# Reaction mechanism and structural evolution of fluorographite cathodes in Li/Na/K batteries

**Zhengping Ding**

Peking University

**Chen Yang**

Peking University

**Cheng Jiang**

School of Materials and Energy, University of Electronic Science and Technology of China

**Shulin Chen**

Peking University

**Ke Qu**

Peking University

**Xiumei Ma**

Peking University

**Jingmin Zhang**

Peking University

**Jing Lu**

State Key Laboratory for Mesoscopic Physics and School of Physics, Peking University, Beijing 100871

**Weifeng Wei**

Central South University <https://orcid.org/0000-0002-3088-6549>

**Peng Gao** (✉ [p-gao@pku.edu.cn](mailto:p-gao@pku.edu.cn))

International Center for Quantum Materials, and Electron Microscopy Laboratory, School of Physics, Peking University <https://orcid.org/0000-0001-9868-2115>

**Liping Wang**

University of Electronic Science and Technology of China

---

## Article

**Keywords:** Fluorographites (CF<sub>x</sub>), Li/Na/K batteries

**Posted Date:** July 15th, 2020

**DOI:** <https://doi.org/10.21203/rs.3.rs-39097/v1>

**License:**   This work is licensed under a Creative Commons Attribution 4.0 International License.

[Read Full License](#)



# Abstract

Fluorographites ( $\text{CF}_x$ ) are potential cathode materials for alkaline metal primary batteries with ultrahigh energy densities. To elucidate the reaction mechanism and structural evolution of  $\text{CF}_x$  cathodes, we combine *in situ* transmission electron microscopy and *ab initio* calculations and discover a two-phase mechanism upon Li/Na/K ion insertion. Amorphous LiF (crystalline NaF and KF nanoparticles) are generated uniformly within the amorphous carbon matrix, which retains an unchanged volume during the discharge process. The diffusivity for K/Na/Li ion migration within the  $\text{CF}_x$  is approximately  $232.9 \text{ nm}^2/\text{s}$ ,  $479.7 \text{ nm}^2/\text{s}$ , and  $2133.0 \text{ nm}^2/\text{s}$ , respectively, which is comparable to the diffusivity of Li/Na/K ions in liquid-state cells. During charging, amorphous LiF and crystal NaF decompose into alkali metal and  $\text{F}_2$ . Our results reveal no substantial volume change and good ion diffusion kinetics, demonstrating the applicability of all-solid-state M/ $\text{CF}_x$  (M = Li/Na/K) primary batteries. This new understanding may promote the design and development of better  $\text{CF}_x$ -based batteries.

While lithium ion batteries (LIBs) are widely applied in portable electronics and electric vehicles, cheaper, more advanced battery systems with higher energy and power densities, and improved safety performance remain in demand.<sup>1-5</sup> Among the materials employed in cathode systems, conversion-type materials, such as halides, chalcogenides, and oxides, demonstrate high specific capacities, offering lithium-metal batteries with high energy densities.<sup>4,6,7</sup> For example, fluorinated graphite ( $\text{CF}_x$ ,  $x = 1$ ) cathodes exhibit a high theoretical energy density and power density of  $3725 \text{ Wh kg}^{-1}$  and  $9313 \text{ Wh L}^{-1}$ , respectively<sup>6</sup>, which can be used in Li primary cells.<sup>8</sup> The practical energy density in Li/ $\text{CF}_{1.0}$  cells reaches  $2600 \text{ Wh kg}^{-1}$ , which is much higher than that in Li/ $\text{I}_2$ , Li/ $\text{SOCl}_2$ , Li/ $\text{MnO}_2$ , Li/ $\text{Ag}_2\text{CrO}_4$ , and Li/ $\text{CuS}$  systems.<sup>9,10</sup>  $\text{CF}_x$  also delivers a discharge specific capacity of  $1061 \text{ mAh/g}$  ( $1439 \text{ Wh kg}^{-1}$ ) with a discharge plateau of  $2.4 \text{ V}$ <sup>11,12</sup> in a Na/ $\text{CF}_x$  system, and  $749 \text{ mAh g}^{-1}$  ( $1869 \text{ Wh kg}^{-1}$ ) with a discharge voltage plateau of  $3.0 \text{ V}$  in a K/ $\text{CF}_x$  system<sup>13</sup>, which makes  $\text{CF}_x$  applicable for multiple alkali ion batteries. Moreover, the irreversible conversion of  $\text{CF}_x$  into LiF and carbon during discharge, due to the high dissociation energy of LiF ( $6.1 \text{ eV}$ ), means the decomposition of LiF by charging alone is not possible.<sup>9,10,12</sup> Yazami et al. first demonstrated the reversible electrochemical reaction of  $\text{CF}_x$  with lithium in F ion batteries with a reversible capacity of  $\sim 120 \text{ mAh g}^{-1}$ .<sup>14</sup> Later, Liu et al. reported a reversible Na/ $\text{CF}_x$  battery with a specific capacity of  $786 \text{ mAh g}^{-1}$ .<sup>11</sup> However, these batteries suffer from poor rate performance at low temperatures<sup>15</sup>, initial voltage delay during the discharge process<sup>8</sup> and large heat generation at high discharge rates, which limit their application in harsh environments.<sup>9,16</sup> Therefore, a detailed study of the reaction mechanisms is urgently required for the further optimization.

Various studies have been conducted to understand these battery systems using different techniques.<sup>8,16-20</sup> For example, *in situ* XRD results suggested a simultaneous formation of a  $\text{CF}_{(x-y)}\text{-Li}^+$  intermediate phase and crystal LiF<sup>15,18</sup>, while other studies reported a formation of amorphous LiF followed by recrystallization to crystalline LiF.<sup>17,19</sup> The crystalline LiF is generated in an orientation that relates to the

absorption energy of the solvents on the LiF surface.<sup>16</sup> The reversibility and reaction mechanism of  $\text{CF}_x$  in Na/ $\text{CF}_x$  batteries was studied using softX-ray absorption spectroscopy (SXAS) and nuclear magnetic resonance (NMR) techniques, which revealed reversible conversions between  $\text{CF}_x$  and NaF.<sup>12</sup> The liquid electrolyte was reported to act as an ion conductor and solution medium to dissolve and aggregate alkali fluoride crystals in a M- $\text{CF}_x$  (M = Li, Na, and K) system, resulting in large crystalline alkali fluorides.<sup>13</sup>

Despite intensive efforts focusing on the reaction mechanism, the structural evolution and reaction pathway of  $\text{CF}_x$  in Li/Na/K batteries remains unclear. In this study, we use *in situ* transmission electron microscopy (TEM) with high spatial/temporal resolution to probe the phase transformation, intermediate phase, and volume change in real time (**Figure 1a**).<sup>21,22</sup> We find that a two-phase reaction occurs during alkali ion intercalation, and the diffusivity of K/Na/Li ion intercalation in  $\text{CF}_x$  is approximately 232.9  $\text{nm}^2/\text{s}$ , 479.7  $\text{nm}^2/\text{s}$ , and 2133.0  $\text{nm}^2/\text{s}$ , respectively. *In situ* electron diffraction patterns show the formation and even distribution of crystalline KF and NaF nanoparticles and amorphous LiF in the amorphous carbon matrix, leading to no volume change. Upon the insertion of K with a large ionic radius, the interlayer spacing of CF increases, and while only subtle changes are observed during Na/Li ion insertion, both are confirmed through density functional theory (DFT) calculations. Moreover, we find both amorphous LiF and crystalline NaF decompose into alkali metal and  $\text{F}_2$  during the charging process under vacuum. The results show no volume change and good ion diffusion kinetics during ion intercalation, suggesting that the all-solid-state M/ $\text{CF}_x$  (M = Li/Na/K) primary batteries have broad applicability.

## Results

**Bulk Structure and Electrochemical Performance of** . The bulk structure of the  $\text{CF}_x$  materials was characterized using XRD, TEM, SAED, HAADF-STEM imaging, and EDS mapping. As shown in **Figure S1**, F atoms bond with C atoms in an  $\text{sp}^3$  hybrid structure; the C atoms have a cyclohexane chair-type structure with AA stacking in the  $\text{CF}_x$  structure.<sup>13,23</sup> **Figure 1b** shows a typical XRD pattern of the  $\text{CF}_x$  sample with the broad diffraction peaks representing the disordered phase. The peak at  $13^\circ$  is assigned to the (002) reflection of the  $\text{CF}_x$ .<sup>9,10,24</sup> The peak at  $41^\circ$  corresponds to (100) and (011) reflections, which is related to the C-C bond length and CF interlayer distance. **Figure 1c** shows a typical TEM bright field image of the  $\text{CF}_x$  material with large sheet-like topography, and the corresponding high resolution TEM image (**Figure 1d**) shows a disordered amorphous structure. As shown in **Figure 1e**, there are two diffraction rings representing the (100), (011) and (110) planes of  $\text{CF}_x$  in the SAED pattern, which is consistent with the XRD results. As shown in the HAADF-STEM image and corresponding color mixed EDS mapping of the  $\text{CF}_x$  sample (**Figure S2**), C and F distribution are uniform in the sample.

Next, we tested  $\text{CF}_x$  ( $x = 0.88$ ) as a cathode material for K-ion batteries (KIBs), Na-ion batteries (SIBs), and LIBs, and typical discharge curves are shown in **Figure 1f**. Under the same  $\text{CF}_x$  discharge current, the KIBs, NIBs, and LIBs discharge specific capacities are  $796.1 \text{ mAh g}^{-1}$ ,  $770.6 \text{ mAh g}^{-1}$ , and  $741.6 \text{ mAh g}^{-1}$ ,

respectively, and the discharge plateaus are  $\sim 2.7$  V,  $\sim 2.6$  V, and  $\sim 2.4$  V, respectively, which is in agreement with our previous work.<sup>13</sup> As the ionic radius of K, Na, and Li is 138 pm, 102 pm, and 76 pm, respectively, the discharge rate specific capacity of Li-ion electrode materials is normally larger than that of Na- and K-ion materials because of the higher mobility of  $\text{Li}^+$ .<sup>25,26</sup> However, the inverse phenomenon of this electrochemical performance is observed, when using  $\text{CF}_x$  as the cathode in KIBs, NIBs, and LIBs, probably due to the Stokes' radius and electrolyte-assisted reaction mechanism.

**Ion Migration Kinetics of K/Na/Li Insertion.** The real time K/Na/Li ion insertion mobility and reaction mechanism of the  $\text{CF}_x$  cathode was studied using the *in situ* all-solid-state nanobattery TEM technique (**Figure 1a**), which has been applied to study the reaction mechanism of electrode materials for batteries at high resolution.<sup>26,27</sup> We used  $\text{M}/\text{M}_2\text{O}$  ( $\text{M} = \text{K}, \text{Na}, \text{and Li}$ ) on a W tip as the counter electrode/solid electrolyte and  $\text{CF}_x$  on a lacey carbon Cu TEM grid as the active electrode for *in situ* experiments. **Figure 2, Figure 3, Figure S36, and Movie S1-3** show the real time *in situ* time series images and analysis results during K/Na/Li ion transport in a nano-sized  $\text{CF}_x$  sample. As shown in **Figure 2a and Movie S1**, K uniformly intercalates into the  $\text{CF}_x$  during the discharge process and the projected area of the entire sample is almost unchanged (**Figure 2d**), suggesting no volume change during potassiation. Upon K intercalation, a clear phase boundary can be seen between pristine  $\text{CF}_x$  and the reacted domain in **Figure 2a**. The two phase boundaries are more obvious in **Figure S3**, which shows the STEM-EDS elemental mapping of C, F and K. The two-phase reaction mode is further confirmed by electron diffraction patterns. As shown in **Figure 3b**, comparing the SAED pattern of unreacted region (I) with the SAED pattern of region II, the additional rings that arise due to diffraction from KF can be seen. The SAED pattern after potassiation suggests that  $\text{CF}_x$  converted to KF and C, which is the same as previous work.<sup>13</sup> **Figure 3c** shows the high resolution TEM (HRTEM) images of  $\text{CF}_x$  after potassiation. The C product maintains amorphous features, and KF nanoparticles ( $\sim 4$  nm) are formed and uniformly distributed in the amorphous carbon matrix. Furthermore, considering the HAADF image contrast is roughly proportional to  $Z^{1.7}$  ( $Z$  represents the atomic number), it was possible to confirm the two-phase boundary using a video taken with *in situ* HAADF-STEM imaging. **Figure S6a–d** shows a series of real time HAADF-STEM images, the raw video is shown in **Movie S4**. As shown in **Figure S6b**, the brighter domain represents the reaction area with K ion intercalation, and the darker domain represents the pristine area. As shown in **Movie S4**, movement of the phase boundary was observed during K ion insertion, and this clear phase boundary is characterized using EDS mapping and EDS spectra (**Figure S6e–h**). Due to an increasing projected reaction area during the phase boundary motion, the K ion diffusivity in  $\text{CF}_x$  is estimated to be  $\sim 232.9$   $\text{nm}^2/\text{s}$  in **Figure 2d**, based on the equation  $D = d^2/t$ , where  $D$  is ion diffusivity,  $d^2$  is the projection area, and  $t$  is the diffusion time.<sup>28</sup>

Sodiation of the  $\text{CF}_x$  sample exhibits a similar two-phase response, as shown in **Figure 2b, 3d–f, S4 and S6i–p, and Movie S3, S5**. Observing the TEM and HAADF-STEM images, we conclude that the volume of  $\text{CF}_x$  remains unchanged after sodiation (**Figure 2e**), and the SAED pattern (**Figure 3e**) shows a two-phase reaction representing the transformation of  $\text{CF}_x$  to NaF and C, which is in agreement with previous

studies.<sup>29,30</sup> After Na intercalation, 6–7 nm NaF nanoparticles are evenly distributed in the amorphous carbon matrix (**Figure 3f**). A two-phase boundary is observed in the elemental mapping of C, F, and Na (**Figure S6m–o**), and the Na ion diffusivity is  $\sim 479.7 \text{ nm}^2/\text{s}$ , as calculated using the projected reaction area (**Movie S2, Figure 2e**). As a parallel comparison, the reaction of  $\text{CF}_x$  with  $\text{Li}^+$  was also examined through *in situ* TEM, and the raw data are shown in **Movie S3, Figure 2c, 2d and Figure S5**. Upon Li ion intercalation, the projected area of  $\text{CF}_x$  remained the same and become smaller (because of sample rotational movement), indicating the volume remains unchanged. According to STEM-EDS mapping (**Figure S4**), C and F are remained uniformly distributed, suggesting no product aggregation phenomena. The two-phase boundary moves fast but is still clear, and the Li ion diffusivity is  $\sim 2133.0 \text{ nm}^2/\text{s}$ , as calculated using the projected reaction area (**Movie S3**). As shown in **Figure S5f–g**, the EELS Li K edge and F K edge spectra are in agreement with that reported for  $\text{LiF}$ ,<sup>31</sup> suggesting that  $\text{LiF}$  is formed after Li ion intercalation. However, in the SAED pattern of pristine  $\text{CF}_x$  (region V) and after lithiation (region VI) (**Figure 3h**), the rings of region VI could be assigned to (111), (220), and (311) of  $\text{Li}_2\text{O}$ , indicating that  $\text{Li}_2\text{O}$  is formed after lithiation. As shown in **Figure 3i**,  $\text{Li}_2\text{O}$  nanoparticles with a size of  $\sim 3 \text{ nm}$  are uniformly distributed in the amorphous carbon matrix after lithiation. According to previous work,  $\text{LiF}$  crystals have been formed and detected using XRD analysis and NMR spectra in liquid Li ion primary batteries during discharge process.<sup>8,9,13,16,17</sup> Considering the all-solid-state environment in *in situ* TEM, amorphous  $\text{LiF}$  is formed in the solid-state  $\text{Li-CF}_x$  system, which is consistent with that reported by Rangasamy.<sup>32</sup> As for the formed  $\text{Li}_2\text{O}$ , Li will diffuse along the surface of the materials during *in situ* TEM, and the active Li will react with trace  $\text{O}_2$  in the TEM instrument, resulting in  $\text{Li}_2\text{O}$  formation in  $\text{CF}_x$ .

Upon formation of a solid-state  $\text{M-CF}_x$  *in situ* TEM system, all alkali ions uniformly diffuse across the materials, with diffusivities of  $232.9 \text{ nm}^2/\text{s}$ ,  $479.7 \text{ nm}^2/\text{s}$ , and  $2133.0 \text{ nm}^2/\text{s}$  for K, Na, and Li ion insertion in  $\text{CF}_x$ , respectively. However, in the liquid electrolyte, the discharge specific capacities of  $\text{CF}_x$  for KIBs, NIBs and LIBs are  $796.1 \text{ mAh g}^{-1}$ ,  $770.6 \text{ mAh g}^{-1}$ , and  $741.6 \text{ mAh g}^{-1}$ , respectively, indicating that the ion mobility of K is higher than that of Na and Li. In the liquid-state  $\text{M-CF}_x$  system, large fluoride crystals are formed and a higher  $\text{K}^+$  diffusivity than  $\text{Na}^+$  and  $\text{Li}^+$  was observed ( $10^{-14}$ - $10^{-10} \text{ cm}^2\text{s}^{-1}$  for  $\text{K}^+/\text{Na}^+$  diffusion and  $10^{-15}$ - $10^{-11} \text{ cm}^2\text{s}^{-1}$  for  $\text{Li}^+$  diffusion).<sup>13</sup> However, if organic solvent molecules are absent from a solid-state battery system, the ion diffusivity is determined by alkali ion insertion ability, as demonstrated by the high ion diffusivities observed for the Li ion in our study using *in-situ* TEM.

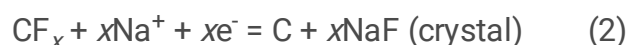
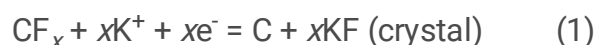
To further understand the alkali ion intercalation behavior in  $\text{CF}_x$ , DFT is applied to calculate the structure and physical-chemical properties after Li/Na/K ion intercalation (**Figures S7–10**). As shown in **Figure S8**, the binding energies for Li, Na, and K adsorption in  $\text{C}_4\text{F}_4$  at high concentrations of  $\text{M}_2\text{C}_4\text{F}_4$  are 4.80 eV, 2.49 eV, and 0.45 eV, respectively, which indicates  $E_b(\text{Li}) > E_b(\text{Na}) > E_b(\text{K})$ . This relationship is the same as results reported by Yoon<sup>33</sup> and our previous work<sup>13</sup>. A high bind energy leads to a high ionic conductivity, which is consistent with our experimental results ( $2133.0 \text{ nm}^2/\text{s}$  for Li,  $479.7 \text{ nm}^2/\text{s}$  for Na, and  $232.9 \text{ nm}^2/\text{s}$  for K). The partial density of states of pristine  $\text{CF}$  and Li/Na/K adsorbed  $\text{CF}$  ( $\text{M}_2\text{C}_4\text{F}_4$ ) is also

acquired through DFT calculations and shown in **Figure S9**. Herein, and based on the theoretical calculations, the CF structure is a semiconductor with a bandgap of 2.4 eV, which is consistent with previous work.<sup>33</sup> For a successful application as battery cathodes, good electrical conductivity is important. After adsorption of Li/Na/K in CF, the Fermi level contains various electronic states, indicating improved electric conductivity. As shown in **Figure 1c**, the initial discharge plateau is low, and then increases to the original state as the discharge process progresses, this is related to the increased conductivity resulting from Li/Na/K adsorption. Furthermore, the ion diffusion pathways and energy profiles for the diffusion of Li/Na/K ions in CF are also calculated and shown in **Figure 4**. Diffusion of Li/Na/K ions at the interlayer of CF proceeds via a zigzag pathway (**Figure 4a–b**); the energy diffusion barrier for Li/Na/K ions is 0.137 eV, 0.568 eV, and 1.591 eV, respectively (**Figure 4c–e**). A low energy diffusion barrier indicates a high ionic mobility, which further confirms our experimental results.

**Phase Transformation and Structural Evolution.** As discussed above, different alkali ions resulted in an unchanged volume during the solid-state reaction; alkali fluoride nanoparticles evenly distributed in the carbon matrix were the resultant products. To probe the phase evolution of  $CF_x$  during alkali ion insertion, *in situ* electron diffraction is applied to study the samples during the entire discharge process and the results are shown in **Figure 5**, **Figure S11** and **Movie S6–S8**. **Figure 5a** presents the radial intensity profiles as a function of reaction time retrieved from *in situ* SAED (**Movie S6**) upon K ion intercalation. The original radial intensity profiles are acquired by integrating the intensity of a series of SAED patterns along the  $r$  direction over the full  $2\pi$  range, and the final radial intensity profiles are obtained after background subtraction using the power-law model (**Figure 5a**). Before potassiation, characteristic diffraction rings for  $CF_x$  corresponding to (100), (011) and (110) peaks were observed (**Figure S10a**). As K ion intercalation progresses, several new diffraction rings appeared, initially faint, then becoming stronger with time. In the corresponding radial intensity profiles (**Figure 5a**), new diffraction peaks that become stronger with time appeared, and these new diffraction peaks are assigned to the (200) and (220) planes of KF. As shown in **Figure 5b**, the diffraction peaks for pristine  $CF_x$  remain and shift left over lower distances, indicating the spacing of monolayer CF increased and the C-C bond length increased after K ion intercalation. Moreover, **Figure 5c** shows the full width at half maxima (FWHM) for the KF peak (200), and the corresponding calculated crystal size of KF-based on the Scherrer equation.<sup>34</sup> After potassiation, ~3.3-nm KF nanoparticles are immediately formed, and the particle sizes remain the same with increasing reaction time, which is in agreement with HRTEM results. The formation of KF nanoparticles also demonstrates the migration of F ions during the reaction, implying a conversion reaction occurs during potassiation. As a parallel comparison, the reaction of  $CF_x$  with Na ions was examined with *in situ* electron diffraction, the raw data from a typical experiment are shown in **Movie S7**. The radial intensity profile and corresponding diffraction patterns with false colors are shown in **Figure 5d–f** and **Figure S10b**. As the Na ion intercalation progresses, several new diffraction rings which could be indexed to the cubic NaF (space group  $Fm-3m$ ), appeared, faint initially and becoming stronger with time. As shown in **Figure 5e**, and different to Na ion insertion, the  $CF_x$  diffraction peak for does not shift during Na ion intercalation, suggesting the spacing of the carbon monolayer product is unchanged. As shown in **Figure 5f**, ~6.3-nm NaF nanoparticles are formed based on the (200) peak of NaF; their size is retained with an

increasing reaction time. Lithiation of  $CF_x$  exhibits a similar phase evolution phenomenon, and is shown in **Movie S8**, **Figure 5g-i** and **Figure S10c**. Upon Li ion intercalation, several new diffraction rings appear, initially faint, and becoming stronger over time (**Figure S10c**). As shown in **Figure 5h**, as the reaction time increases, new, higher, diffraction peaks appear; these new peaks can all be indexed to the cubic  $Li_2O$  phase (space group  $Fm-3m$ ). Furthermore, the (100), (011), and (110) peak position for the resulting carbon monolayer was maintained with increasing reaction time (**Figure 5h**), implying that the amorphous feature of  $CF_x$  remained unaltered after lithiation. As shown in **Figure 5i**, the  $Li_2O$  nanoparticle size slowly increases from 3 nm to 5 nm, which may account for Li aggregation on the surface. As we know, if amorphous LiF is formed in a solid-state Li- $CF_x$  system, no LiF crystal diffraction rings are detected during *in situ* electron diffraction. During K/Na/Li intercalation, the original diffraction peaks for the (100) and (011) planes change, which is connected to the embedded ion structure. **Figure S7a** shows the optimized structure of  $M_2C_4F_4$  which is calculated using DFT. As shown in **Figure S7a**, the distance of the CF monolayer for pristine  $C_4F_4$  is 5.574 Å, and becomes larger, 6.288 Å, 6.592 Å, and 7.285 Å, after Li/Na/K ion insertion, respectively. The corresponding diffraction profile is calculated using CrystalDiffract software based on the optimized structure and is shown in **Figure S7b**. The peak position for the (100) and (011) plane shifts to the right with increased distance after K ion insertion, while the peak position remains unchanged for Na ion insertion, which is consistent with experimental results. Remarkably, the peak position shift left due to the transformation from chair configuration to a flat graphite-like structure during Li intercalation, which is in accordance with *in-situ* experiments and as reported in previous studies.<sup>13,35</sup>

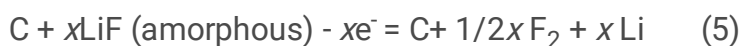
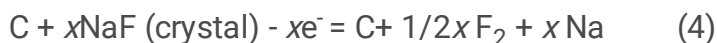
As mentioned above, the electrochemical solid-state reaction of  $CF_x$  with alkali metal ions is expected to behave according to the following equation:



This reaction formula is similar to that of liquid-state batteries, the only difference being that crystalline LiF is produced in the liquid-state mode. Upon K/Na/Li ion insertion, the resulting carbon monolayer maintains its amorphous features. However, the  $CF_x$  monolayer distance becomes larger with ion insertion, resulting in (100) and (011) peak shifts during K ion intercalation. In liquid-state batteries, the alkali fluoride will dissolve and then aggregate on the  $CF_x$  surface, resulting in large crystals (~200–300 nm) and theoretical volume expansion of the electrode (56.9% for K insertion, 32.9% for Na insertion, 22.9% for Li insertion).<sup>8,11,13</sup> However, in the solid-state system, alkali fluoride nanoparticles are formed immediately and the size of the alkali fluoride nanoparticles remains unchanged with time. As the alkali fluoride nanoparticles are uniformly distributed in the amorphous carbon matrix and the size remains unchanged during the reaction, volume expansion does not occur, which is beneficial for solid-state

battery systems. Furthermore, the diffusivity is 232.9 nm<sup>2</sup>/s ( $2.329 \times 10^{-12}$  cm<sup>2</sup>/s), 479.7 nm<sup>2</sup>/s ( $4.797 \times 10^{-12}$  cm<sup>2</sup>/s), and 2133.0 nm<sup>2</sup>/s ( $2.133 \times 10^{-11}$  cm<sup>2</sup>/s) for K, Na, and Li ion insertion, respectively, in solid CF<sub>x</sub> cells, which is comparable to the diffusivity of Li/Na/K ions in liquid-state alkaline cells ( $10^{-14}$ – $10^{-10}$  cm<sup>2</sup> s<sup>-1</sup> for K<sup>+</sup>/Na<sup>+</sup> diffusion and  $10^{-15}$ – $10^{-11}$  cm<sup>2</sup> s<sup>-1</sup> for Li<sup>+</sup> diffusion)<sup>13</sup>, this also indicates that CF<sub>x</sub> is a suitable cathode for solid-state cells. In order to test the electrochemical performance as a cathode in a solid-state battery, the solid-state Li/PEO-LiTFSI/CF<sub>x</sub> cell is fabricated using PEO-LiTFSI as the solid electrolyte. As shown in **Figure S11**, the discharge capacity of the solid-state Li/PEO-LiTFSI/CF<sub>x</sub> cell is 507.4 mAh g<sup>-1</sup> (1215.4 Wh kg<sup>-1</sup>) at room temperature with a discharge current of 0.02C, indicating that CF<sub>x</sub> can be used as a cathode material for high energy density solid-state primary batteries.

**Na/Li Extraction Reaction Mechanism.** As LiF cannot be electrochemically decomposed merely, it is widely accepted that the reaction of CF<sub>x</sub> with lithium is likely irreversible, meaning Li/CF<sub>x</sub> can only be used as a primary cell. However, recently, a reversible charge/discharge capacity of 786 mAh/g for a Na/CF<sub>x</sub> system was achieved, illustrating that CF<sub>x</sub> is a promising cathode material for SIBs.<sup>11</sup> To investigate the Na ion extraction reaction mechanism of CF<sub>x</sub>, *in situ* TEM is applied to study the samples during the entire charge process, the raw data and analysis results are shown in **Figure 6a–e**, **Figure S12** and **Movie S9**. As shown in **Figure 6a**, no phase boundaries occur during Na ion extraction. From 431 s to 435 s, the NaF product homogeneously and immediately decomposed under a 5-V charge, which is further confirmed by the SAED patterns. Before desodiation, the diffraction rings in **Figure 6c** can be index to NaF. After desodiation, the diffraction rings of NaF disappear, and the remaining diffraction rings in **Figure 6e** can be index to amorphous carbon, which has same features as that of pristine CF<sub>x</sub>. As shown in the HRTEM images (**Figure 6b**), NaF nanoparticles are evenly distributed in the amorphous carbon matrix before the charge process, during Na ion extraction NaF decomposes leaving amorphous carbon (**Figure 6d**). **Figure S12** shows the HAADF-STEM image and corresponding EDS spectrum and elemental mapping of CF<sub>x</sub> after sodiation and desodiation. Comparing the disappearance of Na and F after the charging process indicates NaF decomposes into Na, which returns to the Na/Na<sub>x</sub>O probe, and F<sub>2</sub>, which evaporates into the vacuum system. Delithiation of CF<sub>x</sub> during the charging progress exhibits a similar decomposition phenomenon, as shown in **Movie S10**, **Figure 6f–j** and **Figure S13**. As shown in **Figure 6f**, there are also no phase boundaries during Li extraction. According to the SAED pattern in **Figure 6h–j**, the Li<sub>2</sub>O nanoparticles on the CF<sub>x</sub> surface all decompose following delithiation, which is further verified by the HRTEM images in **Figure 6g–i**. Interestingly, the F disappears from the STEM-EDS mapping and EDS spectrum, suggesting all the amorphous LiF decomposes into Li and F<sub>2</sub> under a 5 V charge. The electrochemical solid-state reaction of CF<sub>x</sub> with Na/Li ions during the charging process is expected to behave according to the following equations:



As discussed above, the *in situ* all-solid-state nanobattery TEM technique was employed to explore the reaction mechanism of  $\text{CF}_x$  with K/Na/Li during ion intercalation/extraction. In the M/ $\text{CF}_x$  liquid-state battery, the K ion diffusivity is higher than that of Li and Na ions, and the discharge products are amorphous carbon and large alkali fluoride crystals. In the solid-state battery system, the alkali ion intercalation reaction mechanism is significantly different from that of the liquid-state system, see **Figure 7**. In the M/ $\text{CF}_x$  solid-state battery system, a two-phase reaction and phase boundary movement (**Figure 2–3**) is observed during alkali ion intercalation. Based on the two-phase boundary movement (**Figure 2**), the diffusivity of K/Na/Li ion intercalation in  $\text{CF}_x$  is 232.9  $\text{nm}^2/\text{s}$ , 479.7  $\text{nm}^2/\text{s}$ , and 2133.0  $\text{nm}^2/\text{s}$ , respectively, which is further investigated through DFT calculations (**Figure 4**). According to the *in situ* electron diffraction results (**Figure 5**), crystalline KF, NaF nanoparticles, and amorphous LiF are formed and remain unchanged with increasing reaction time; furthermore, these alkali fluoride nanoparticles are uniformly distributed in the amorphous carbon matrix, resulting in no volume change. During the charging progress in the solid-state cell (**Figure 6**), the NaF product decomposes into Na and  $\text{F}_2$ , leading to the possibility of a reversible Na/ $\text{CF}_x$  battery, which is in agreement with previous studies.<sup>11, 12, 40, 45</sup> Converse to the understanding that the charging-induced decomposition of LiF is not possible, our observations show LiF simultaneously dissociates into  $\text{F}_2$  and Li following charging. According to the volume expansion limit and high ion diffusivity, the all-solid-state Li/PEO-LiTFSI/ $\text{CF}_x$  cell possess a discharge capacity of 507.4  $\text{mAh g}^{-1}$  with a high energy density of 1215.4  $\text{Wh kg}^{-1}$  at room temperature (**Figure S11**).

## Methods

**Electrochemical Characterization:** Fluorinated graphite  $\text{CF}_{0.88}$  was purchased from Hubei Zhuoxi Fluorochemical Co., LTD, China and used without further purification. Powder X-ray diffraction patterns were obtained using a Bruker AXS D8 Advance X-ray diffractometer (Germany) with a step size of  $0.02^\circ$  at a dwell time of 1 s. The  $\text{CF}_{0.88}$  materials were mixed with acetylene black and polyvinylidene fluoride binder at a weight ratio of 7:2:1 and then dissolved completely in N-methyl-2-pyrrolidone. After stirring for 1 h, the obtained slurry was homogeneously pasted onto Al foil and dried at  $110^\circ\text{C}$  for 12 h in a vacuum oven. The coated foil was cut into circular pieces with a diameter of 12 mm. A cathode electrode, a separator (glass fiber), and a metallic anode (K, Na, Li) were assembled into a coin-type half-cell (CR 2032) in an Ar-filled glove box (MBraun, Germany). The electrolyte solution was prepared by dissolving 1 M  $\text{APF}_6$  (A = K, Na, Li) in ethylene carbonate/dimethyl carbonate (1:1, v/v). The discharge tests were performed using a LANHE CT2001A cell test system at room temperature to 1.5 V at a constant current rate of 0.02C (1C = 821 mA/g). For the solid Li cell, the separator film was replaced with glass fiber, and LiTFSI-PEO (Li/EO = 20:1 mol/mol) was used as a solid electrolyte.

***In Situ* TEM:** *In situ* TEM, high-angle annular dark field (HAADF), and selected area electron diffraction (SAED) were carried out using a Tecnai F20 at 200 kV equipped with an Oneview IS (Gatan) camera. **Figure 1a** shows a schematic illustration of the *in situ* TEM experimental procedure. The *in situ* TEM

electrochemical cell was incorporated into an electrical TEM specimen holder (PicoFemto, China), where  $\text{CF}_{0.88}$  was dispersed on a TEM half Cu-grid with a lacey carbon support acting as the active electrode material, current collector, and conductive carbon; alkali metal (Li/Na/K) was coated on an electrochemically etched sharp tungsten probe and acted as the counter electrode. During the transfer process, the active alkali metal probe was intentionally exposed to the air (less than 10 s) to form a  $\text{M}_x\text{O}$  ( $\text{M} = \text{Li}, \text{Na}, \text{and K}$ ) layer on the alkali metal surface, the formed  $\text{M}_x\text{O}$  acts as a solid-state electrolyte. A constant negative potential (-3 V) was applied between  $\text{CF}_{0.88}$  and the Li/Na/K source during the discharge process, while a constant positive potential (+5 V) was applied during the charge process.

The high-resolution TEM images, dark field images, and EDS mapping were acquired using a FEI Tecnai F20 with an Oxford X-Max<sup>N</sup> TSR EDS detector. Electron energy loss spectroscopy (EELS) was conducted on an aberration-corrected FEI (Titan Cubed Themis G2) equipped with an X-FEG gun operated at 300 kV with ~50 pA beam current. The EELS data was collected using a Gatan Enfinity system with a collection semi-angle of 5.9 mrad, a convergence semi-angle of 25 mrad and a dispersion of 0.25 eV/ch. The data was processed using DigitalMicrograph (Gatan) software.

**First-Principles Calculations:** The pristine AA-stacking CF structure was used based on our previous work.<sup>13</sup> The Vienna *ab initio* simulation package (VASP) was used to optimize the structure and perform electronic state calculations.<sup>36,37</sup> The 'energy' code in the Cambridge Sequential Total Energy Package (CASTEP) was performed to obtain the precise energies of the materials.<sup>38</sup> These calculations were based on density functional theory (DFT), and generalized gradient approximation (GGA) combined with adoption of the Perdew–Burke–Ernzerhof (PBE) form.<sup>39</sup> The Monkhorst–Pack scheme sampling method with a separation of  $0.02 \text{ \AA}^{-1}$  was used to generate the k-points mesh. The convergence thresholds were set as  $10^{-6}$  eV for energy and  $10^{-3}$  eV/ $\text{\AA}$  for force.

The binding energy ( $E_b$ ) per Li/Na/K atom was defined as  $E_b = (E_{\text{CF}} + xE_{\text{Li/Na/K}} - E_{\text{CF-Li/Na/K}}) / x$ . Herein,  $E_{\text{CF}}$ ,  $E_{\text{Li/Na/K}}$ , and  $E_{\text{CF-Li/Na/K}}$  are the energy of the pristine CF, Li/Na/K adsorbed CF and per Li/Na/K atom in the vacuum, respectively.  $x$  is the number of Li/Na/K atoms adsorbed in the CF. The climbing image nudged elastic band (CI-NEB) method implemented in the VASP transition state tools was used to calculate the Li/Na/K atom diffusion barriers.<sup>40,41</sup> Herein, one Li/Na/K atom was initially adsorbed in the hollow site of the  $3 \times 3 \times 1$  CF supercell (including 36 C and 36 F atoms), based on previous work.<sup>35</sup> Next, the Li/Na/K atom diffused to the adjacent hollow site with the fixed lattice constant  $c$  (perpendicular to the layer plane) of  $12.28 \text{ \AA}$  (the lattice constant of CF<sup>13,35</sup>). Such a supercell was large enough to avoid interactions between Li/Na/K atoms in different supercells and was used to simulate initial diffusion Li/Na/K at low concentrations.<sup>42-44</sup>

## Declarations

**Data availability.** The authors declare that all relevant data are included in the paper and its Supplementary Information files. Additional data including the codes are available from the corresponding author upon reasonable request.

## Acknowledgements

This work was supported by the National Key R&D Program of China (grant no. 2016YFA0300903), National Natural Science Foundation of China (51672007 and 11974023), the Key R&D Program of Guangdong Province (2018B030327001, 2018B010109009), the China Postdoctoral Science Foundation (2019M650333), the International Science and Technology Cooperation Program of China (2014DFE00200). Liping Wang thank the Fundamental Research Funds for the Central Universities, China (ZYGX2019Z008). P. G. gratefully acknowledge the support from the National Program for Thousand Young Talents of China and “2011 Program” Peking-Tsinghua-IOP Collaborative Innovation Center of Quantum Matter. This project was also partly supported by the State Key Laboratory of Powder Metallurgy, Central South University, Changsha, China.

## Author Contributions

Z. D., L. W, and P. G. conceived the idea and directed the research. Z. D. carried out *in situ* TEM, SAED and HADDF measurements, XRD test and analyzed data. C. Y. and J. L. performed the DFT calculations and analyzed the DFT results. C. J. and L. W. performed the battery assembly and electrochemical test. S. C., and K. Q. assisted with data analysis. X. M., J. Z. assisted with TEM measurements. Z. D., L. W. and P. G. co-wrote the paper with input from all authors.

## Competing interests

The authors declare no competing interests.

**Address correspondence:** Z.P. Ding ([zhengpingding@pku.edu.cn](mailto:zhengpingding@pku.edu.cn)), P. Gao ([p-gao@pku.edu.cn](mailto:p-gao@pku.edu.cn)). L. Wang ([lipingwang@uestc.edu.cn](mailto:lipingwang@uestc.edu.cn))

## References

1. Armand, M. & Tarascon, J.M. Building better batteries. *Nature* **451**, 652–7 (2008).
2. Kang, B. & Ceder, G. Battery materials for ultrafast charging and discharging. *Nature* **458**, 190–3 (2009).
3. Tarascon, J.M. & Armand, M. Issues and challenges facing rechargeable lithium batteries. *Nature* **414**, 359 – 67 (2001).
4. Turcheniuk, K., Bondarev, D., Singhal, V. & Yushin, G. Ten years left to redesign lithium-ion batteries. *Nature* **559**, 467–470 (2018).
5. Assat, G. & Tarascon, J.-M. Fundamental understanding and practical challenges of anionic redox activity in Li-ion batteries. *Nat. Energy* **3**, 373–386 (2018).
6. Wang, L.P. *et al.* Li-free Cathode Materials for High Energy Density Lithium Batteries. *Joule* **3**, 2086–2102 (2019).

7. Yu, S.H., Feng, X., Zhang, N., Seok, J. & Abruna, H.D. Understanding Conversion-Type Electrodes for Lithium Rechargeable Batteries. *Acc. Chem. Res.* **51**, 273–281 (2018).
8. Ahmad, Y., Dubois, M., Guérin, K., Hamwi, A. & Zhang, W. Pushing the theoretical limit of Li–CF<sub>x</sub> batteries using fluorinated nanostructured carbon nanodiscs. *Carbon* **94**, 1061–1070 (2015).
9. Zhang, Q., Takeuchi, K.J., Takeuchi, E.S. & Marschilok, A.C. Progress towards high-power Li/CF<sub>x</sub> batteries: electrode architectures using carbon nanotubes with CF<sub>x</sub>. *Phys. Chem. Chem. Phys.* **17**, 22504–18 (2015).
10. Amatucci, G.G. & Pereira, N. Fluoride based electrode materials for advanced energy storage devices. *J. Fluorine Chem.* **128**, 243–262 (2007).
11. Liu, W., Li, H., Xie, J.Y. & Fu, Z.W. Rechargeable room-temperature CF(x)-sodium battery. *ACS Appl. Mater. Interfaces* **6**, 2209–12 (2014).
12. Shao, Y. *et al.* Synthesis and Reaction Mechanism of Novel Fluorinated Carbon Fiber as a High-Voltage Cathode Material for Rechargeable Na Batteries. *Chem. Mater.* **28**, 1026–1033 (2016).
13. Jiang, C. *et al.* Electrolyte-assisted dissolution-recrystallization mechanism towards high energy density and power density CF cathodes in potassium cell. *Nano Energy* **70**(2020).
14. Yazami, R. Fluoride ion electrochemical cell. (Google Patents, 2013).
15. Nagasubramanian, G. & Rodriguez, M. Performance enhancement at low temperatures and in situ X-ray analyses of discharge reaction of Li/(CF<sub>x</sub>)<sub>n</sub> cells. *J. Power Sources* **170**, 179–184 (2007).
16. Long, S. *et al.* Study on Crystal Growth Kinetics and Preferred Orientation for LiF Crystal in Dimethyl Sulfoxide/1,3-Dioxolane-based Electrolyte. *J. Phys. Chem. C* **123**, 28048–28057 (2019).
17. Read, J., Collins, E., Piekarski, B. & Zhang, S. LiF Formation and Cathode Swelling in the Li/CF<sub>x</sub> Battery. *J. Electrochem. Soc.* **158**(2011).
18. Rodriguez, M.A., Keenan, M.R. & Nagasubramanian, G. In situ X-ray diffraction analysis of (CF<sub>x</sub>)<sub>n</sub> batteries: signal extraction by multivariate analysis. *J. Appl. Crystallogr.* **40**, 1097–1104 (2007).
19. Zhong, G. *et al.* Insights into the lithiation mechanism of CF<sub>x</sub> by a joint high-resolution <sup>19</sup>F NMR, in situ TEM and <sup>7</sup>Li NMR approach. *J. Mater. Chem. A* **7**, 19793–19799 (2019).
20. Wang, J. *et al.* Unraveling nanoscale electrochemical dynamics of graphite fluoride by in situ electron microscopy: key difference between lithiation and sodiation. *J. Mater. Chem. A* **8**, 6105–6111 (2020).
21. Yuan, Y., Amine, K., Lu, J. & Shahbazian-Yassar, R. Understanding materials challenges for rechargeable ion batteries with in situ transmission electron microscopy. *Nat. Commun.* **8**, 15806 (2017).
22. Gao, P. Nanosized Cu-Li glass. *Sci. Bull.* **63**, 1173–1174 (2018).
23. Hamwi, A. Fluorine reactivity with graphite and fullerenes. fluoride derivatives and some practical electrochemical applications. *J. Phys. Chem. Solids* **57**, 677–688 (1996).
24. Chronopoulos, D.D., Bakandritsos, A., Pykal, M., Zboril, R. & Otyepka, M. Chemistry, properties, and applications of fluorographene. *Appl. Mater. Today* **9**, 60–70 (2017).

25. Kim, S., Cui, J., Dravid, V.P. & He, K. Orientation-Dependent Intercalation Channels for Lithium and Sodium in Black Phosphorus. *Adv. Mater.* **31**, e1904623 (2019).
26. Boebinger, M.G. *et al.* Avoiding Fracture in a Conversion Battery Material through Reaction with Larger Ions. *Joule* **2**, 1783–1799 (2018).
27. Gao, P. *et al.* High-Resolution Tracking Asymmetric Lithium Insertion and Extraction and Local Structure Ordering in SnS<sub>2</sub>. *Nano Lett.* **16**, 5582–8 (2016).
28. Chen, S. *et al.* Atomic structure and migration dynamics of MoS<sub>2</sub>/Li<sub>x</sub>MoS<sub>2</sub> interface. *Nano Energy* **48**, 560–568 (2018).
29. Liu, W. *et al.* Enhanced electrochemical activity of rechargeable carbon fluorides–sodium battery with catalysts. *Carbon* **93**, 523–532 (2015).
30. Liu, W. *et al.* Amorphous, Highly Disordered Carbon Fluorides as a Novel Cathode for Sodium Secondary Batteries. *J. Phys. Chem. C* **120**, 25203–25209 (2016).
31. Sina, M. *et al.* Direct Visualization of the Solid Electrolyte Interphase and Its Effects on Silicon Electrochemical Performance. *Adv. Mater. Interfaces* **3**, 1600438 (2016).
32. Rangasamy, E., Li, J., Sahu, G., Dudney, N. & Liang, C. Pushing the theoretical limit of Li-CF(x) batteries: a tale of bifunctional electrolyte. *J. Am. Chem. Soc.* **136**, 6874–7 (2014).
33. Yoon, G., Kim, H., Park, I. & Kang, K. Conditions for Reversible Na Intercalation in Graphite: Theoretical Studies on the Interplay Among Guest Ions, Solvent, and Graphite Host. *Adv. Energy Mater.* **7**(2017).
34. Boullay, P., Lutterotti, L., Chateigner, D. & Sicard, L. Fast microstructure and phase analyses of nanopowders using combined analysis of transmission electron microscopy scattering patterns. *Acta Crystallogr. A Found Adv.* **70**, 448–56 (2014).
35. Rao, F., Wang, Z., Xu, B., Chen, L. & Ouyang, C. First-Principles Study of Lithium and Sodium Atoms Intercalation in Fluorinated Graphite. *Engineering* **1**, 243–246 (2015).
36. Kresse, G. & Hafner, J. Ab initio molecular dynamics for liquid metals. *Phys. Rev. B Condens. Matter.* **47**, 558–561 (1993).
37. Kresse, G. & Hafner, J. Ab initio molecular-dynamics simulation of the liquid-metal-amorphous-semiconductor transition in germanium. *Phys. Rev. B Condens. Matter.* **49**, 14251–14269 (1994).
38. Clark, S.J. *et al.* First principles methods using CASTEP. *Zeitschrift für Kristallographie - Crystalline Materials* **220**(2005).
39. John P. Perdew, K.B., and Matthias Ernzerhof. Generalized Gradient Approximation Made Simple. *Phys. Rev. Lett.* **78**(1997).
40. Graeme, H., Blas, P.U. & Harnes, J. A climbing image nudged elastic band method for finding saddle points and minimum energy paths. *J. Chem. Phys.* **113**, 9901–9904 (2000).
41. Graeme Henkelman, H.J. Improved tangent estimate in the nudged elastic band method for finding minimum energy paths and saddle points. *J. Chem. Phys.* **113**, 9978–9985 (2000).
42. Zhang, X. *et al.* Monolayer GaS with high ion mobility and capacity as a promising anode battery material. *J. Mater. Chem. A* **7**, 14042–14050 (2019).

43. Yang, C. *et al.* Ultrahigh Capacity of Monolayer Dumbbell C<sub>4</sub>N as a Promising Anode Material for Lithium-Ion Battery. *J. Electrochem. Soc.* **167**(2020).
44. Yang, C. *et al.* Holey graphite: A promising anode material with ultrahigh storage for lithium-ion battery. *Electrochim. Acta* **346**(2020).

## Figures

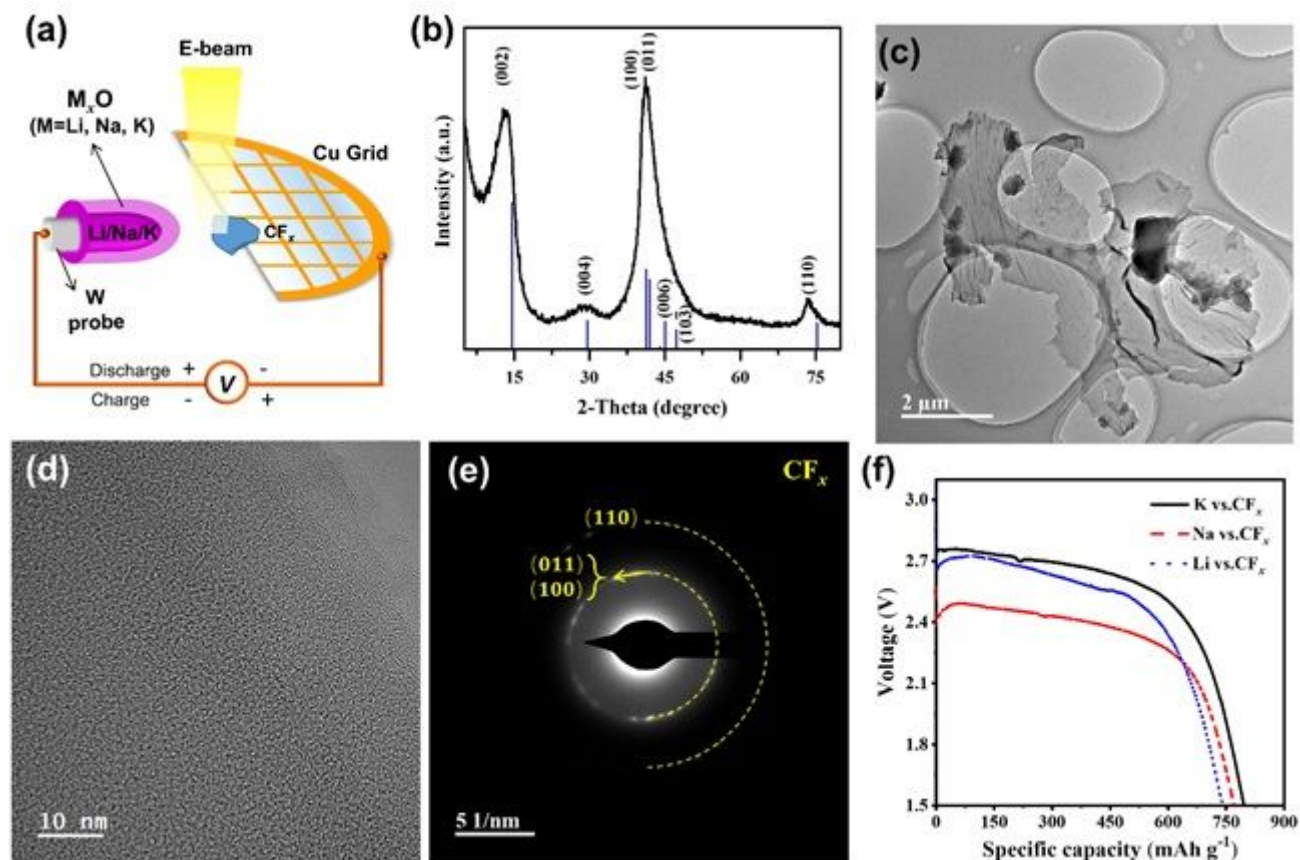


**Figure 1**

Structural characterizations and electrochemical performances of CF<sub>x</sub>. (a) Schematic illustration of the experimental setup for the in-situ TEM experimental procedure, (b) Powder XRD pattern of CF<sub>x</sub>. TEM image (c), HRTEM image (d), and SAED image (e) of CF<sub>x</sub>. (f) Electrochemical measurements of CF<sub>x</sub> in a K cell, Na cell, and Li cell.

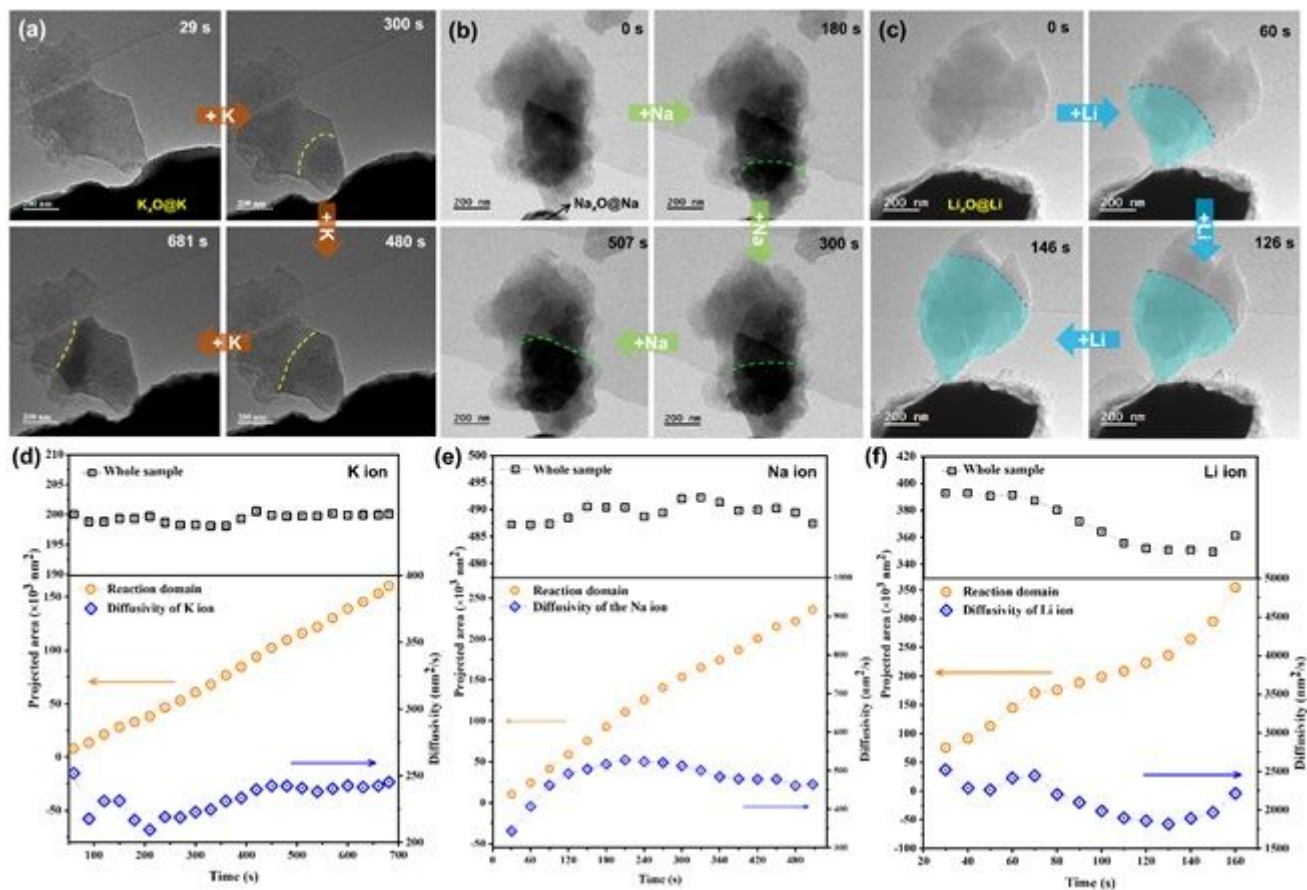


**Figure 2**

Ion migration kinetics of K/Na/Li ion insertion in CFx. Time-sequenced in situ TEM images of CFx during potassiation (a), sodiation (b), and lithiation (c) Projected area of the whole sample and reaction domain, and ion diffusivity are plotted as a function of time calculated from (a) during potassiation (d), sodiation (e), and lithiation (f).

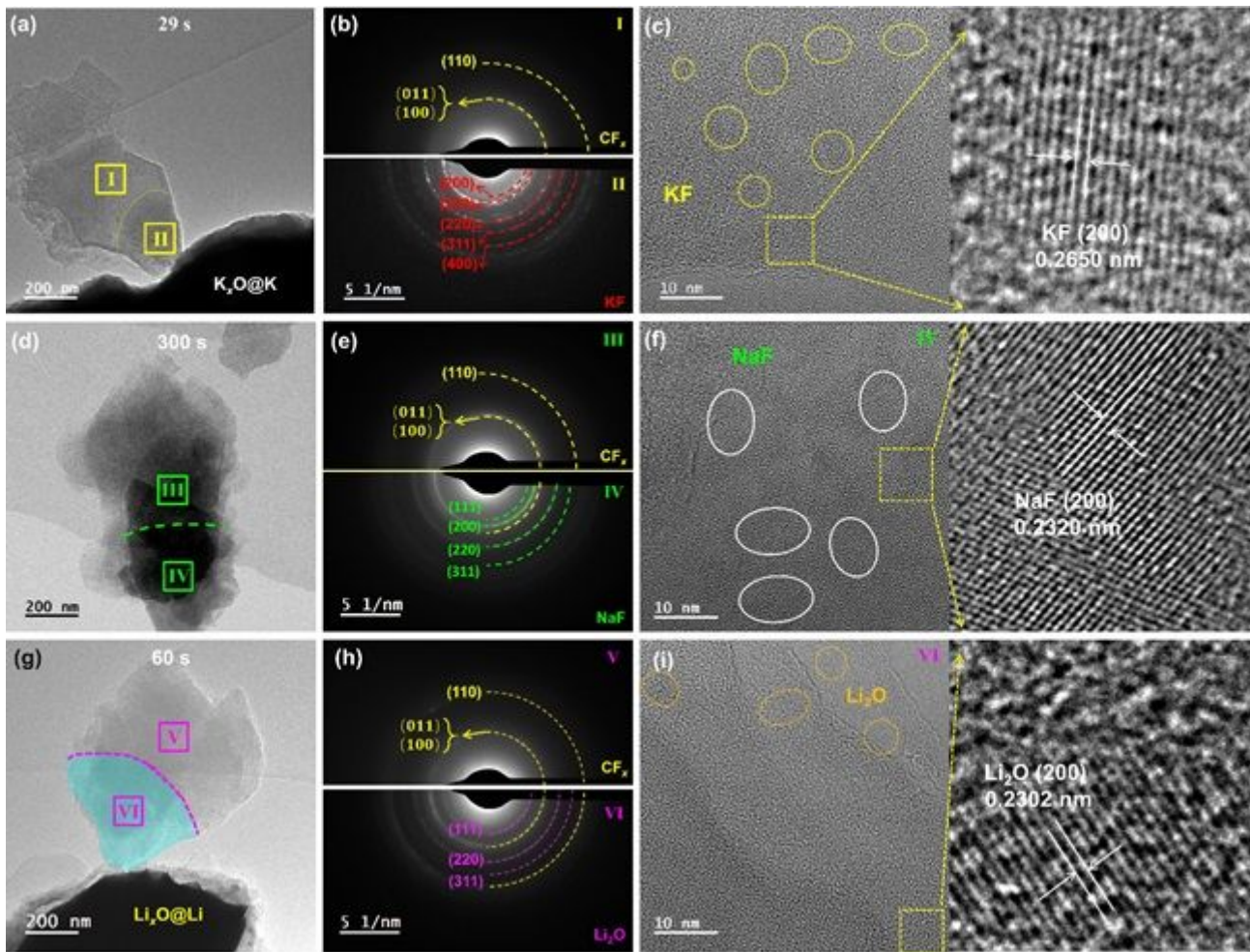


**Figure 3**

Characterization of CF<sub>x</sub> following in situ ion insertion reaction. (a) in situ TEM image of CF<sub>x</sub> during potassiation at 300 s. (b) SAED pattern obtained from pristine CF<sub>x</sub> (I) and reaction region (II). (c) HRTEM images of region II. (d) in situ TEM image of CF<sub>x</sub> during sodiation at 300 s. (e) SAED pattern obtained from pristine CF<sub>x</sub> (III) and reaction region (IV). (f) HRTEM images of region IV. (g) in situ TEM image of CF<sub>x</sub> during lithiation at 60 s. (h) SAED pattern obtained from pristine CF<sub>x</sub> (V) and reaction region (VI). (i) HRTEM images of region VI.

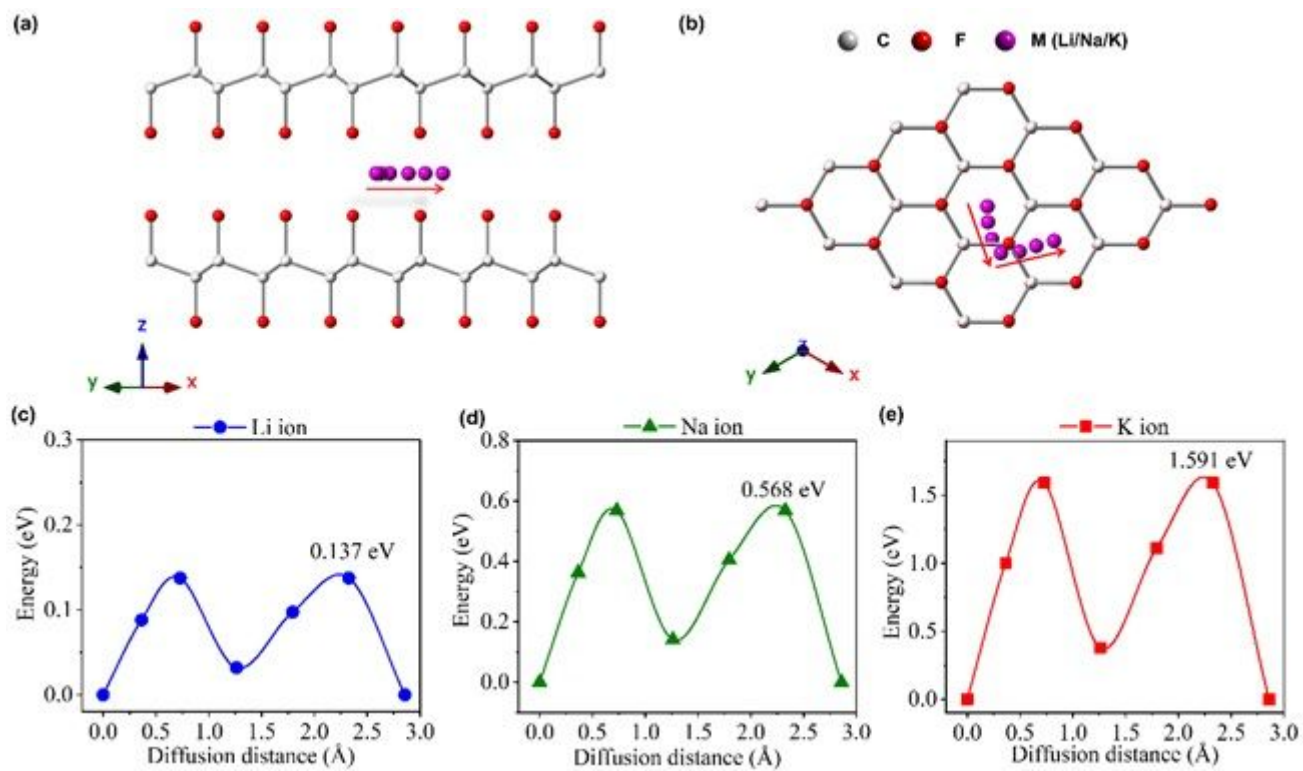


**Figure 4**

Diffusion pathway and energy profiles of Li/Na/K ion diffusion in CF<sub>x</sub>. (a,b) The diffusion pathway of Li/Na/K ions in CF<sub>x</sub>. (c–e) Energy profile of Li/Na/K ion diffusion.

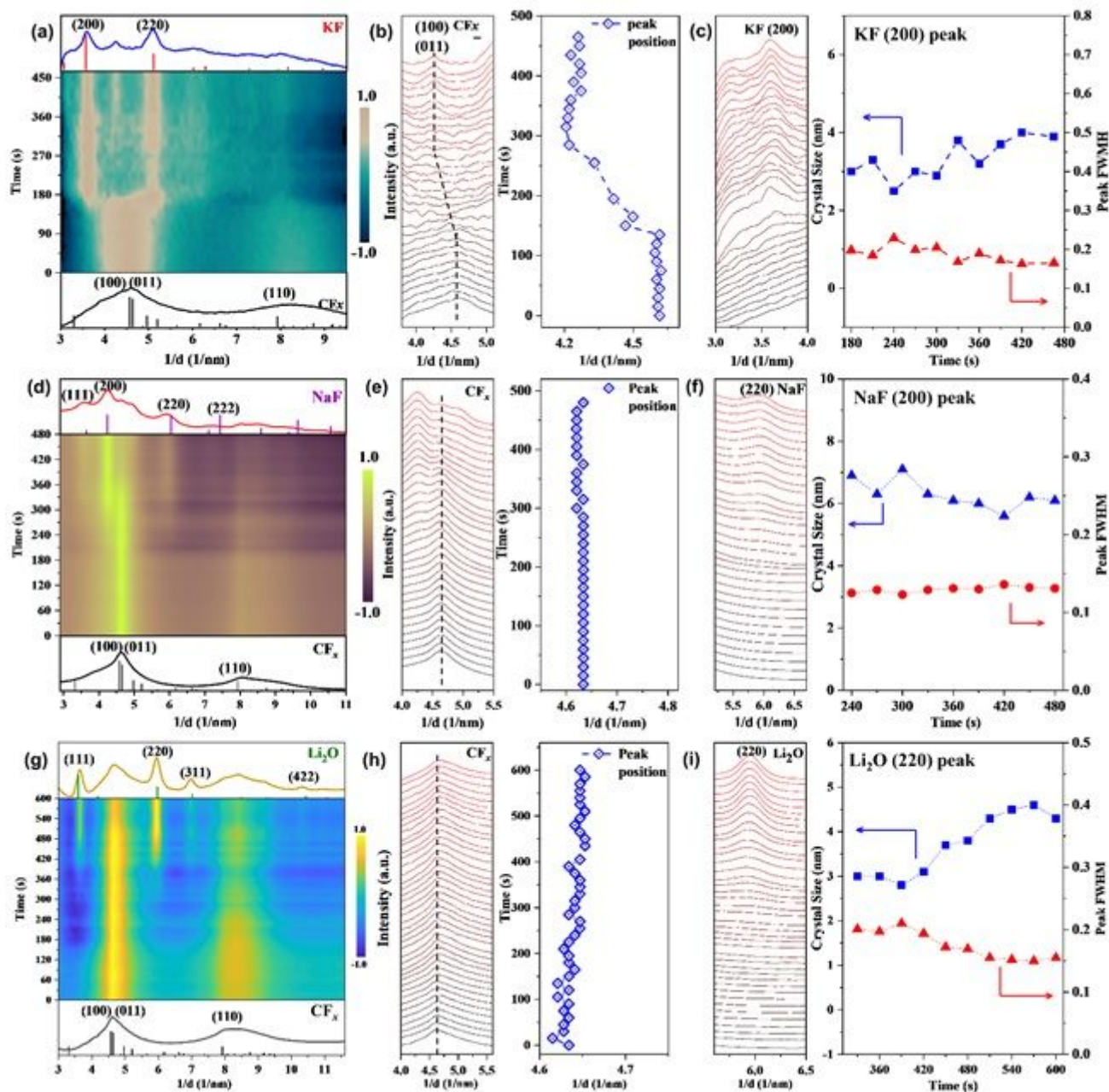


**Figure 5**

Phase evolution tracking using in situ SAED of CF<sub>x</sub>. (a) In situ SAED intensity profile and (b) peak position of CF<sub>x</sub> as a function of reaction time during potassiation. (c) Full width at half maxima (FWHM) for the KF peak (200), and the corresponding calculated crystal size of KF-based on the Scherrer equation. (d) In situ SAED intensity profile and (e) peak position of CF<sub>x</sub> as a function of reaction time during sodiation. (f) FWHM for the NaF peak (200), and the crystal size of NaF. (g) In situ SAED intensity profile and (h) peak position of CF<sub>x</sub> as a function of reaction time during lithiation. (i) FWHM for the Li<sub>2</sub>O peak (220), and the crystal size of Li<sub>2</sub>O.

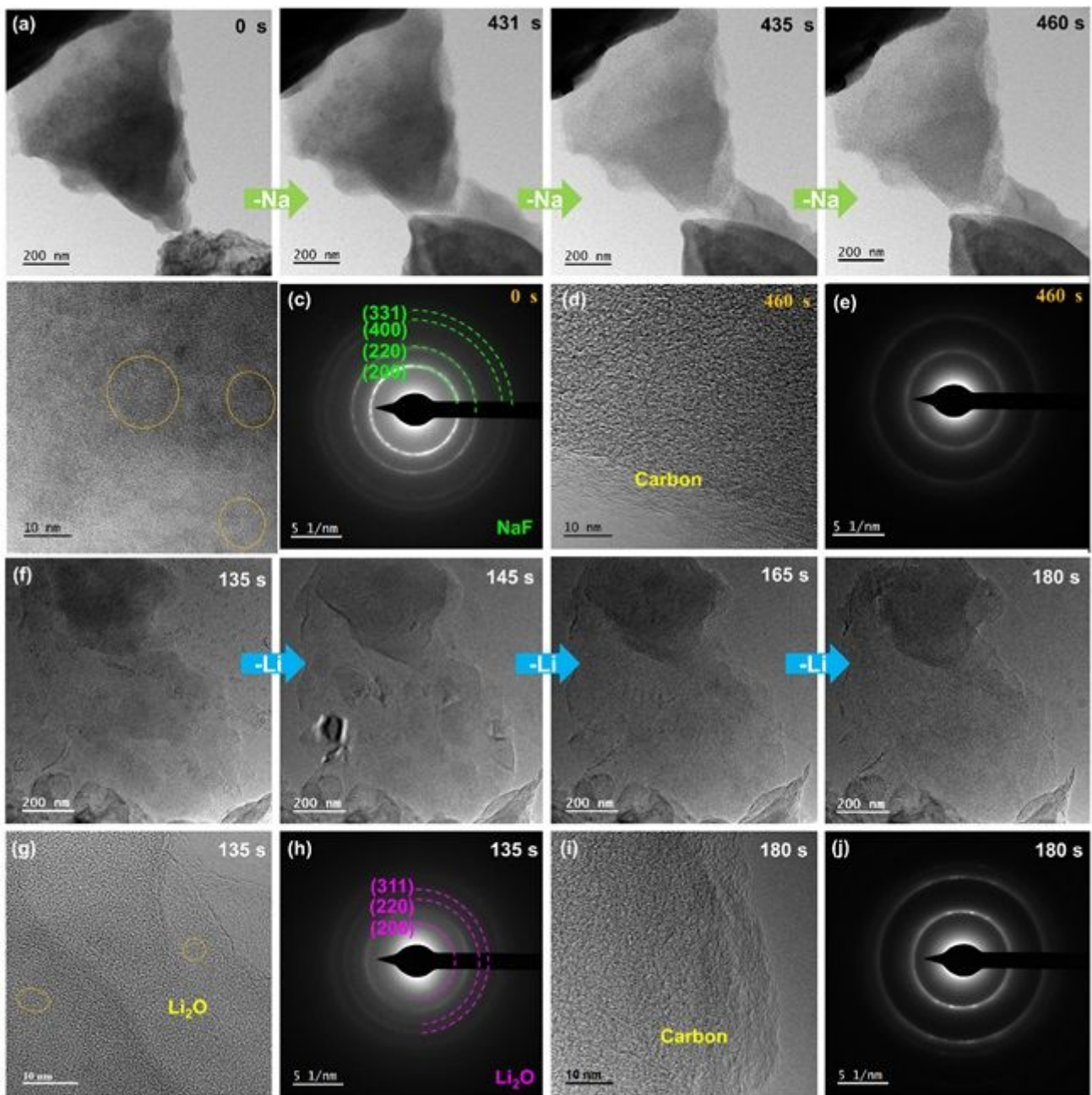


**Figure 6**

Alkali ion extraction. Time-sequenced in situ TEM images (a) during Na ion extraction of CF<sub>0.88</sub>. HRTEM images of CF<sub>x</sub> after sodiation (b) and desodiation (d) SAED pattern of CF<sub>x</sub> after sodiation (c) and desodiation (e) Time-sequenced in situ TEM images (f) during Li ion extraction of CF<sub>0.88</sub>. HRTEM images of CF<sub>x</sub> after lithiation (g) and delithiation (i) SAED pattern of CF<sub>x</sub> after lithiation (h) and delithiation (j).

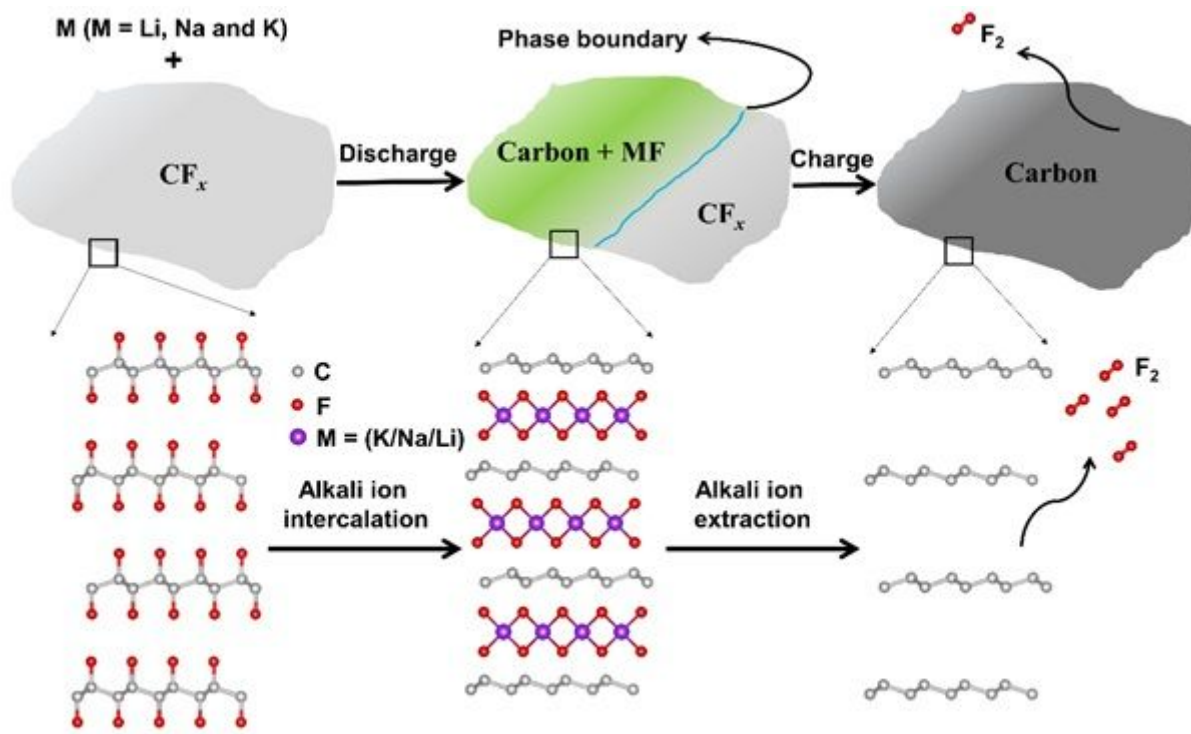


Figure 7

Reaction mechanism schematic of  $CF_x$  and alkali ions (K/Na/Li) during the charge/discharge process in an in situ TEM all solid-state cell.

## Supplementary Files

This is a list of supplementary files associated with this preprint. Click to download.

- [Sl.docx](#)